Pressure-induced structural transition, metallization, and topological superconductivity in PdSSe

Feng Xiao,[1] Wen Lei,[1,2] Wei Wang,[1,3] Carmine Autieri,[4] Xiaojun Zheng,[1] Xing Ming,[1,*] and Jianlin Luo[5,6]

[1]*College of Science, MOE Key Laboratory of New Processing Technology for Nonferrous Metal and Materials, Guilin University of Technology, Guilin 541004, People's Republic of China*

[2]*Key Laboratory of Artificial Micro- and Nano-Structures of Ministry of Education and School of Physics and Technology, Wuhan University, Wuhan 430072, People's Republic of China*

[3]*School of Materials Science and Engineering, Beihang University, Beijing 100191, People's Republic of China*

[4]*International Research Centre MagTop, Institute of Physics, Polish Academy of Sciences, Aleja Lotników 32/46, PL-02668 Warsaw, Poland*

[5]*Beijing National Laboratory for Condensed Matter Physics and Institute of Physics, Chinese Academy of Sciences, Beijing 100190, People's Republic of China*

[6]*School of Physical Sciences, University of Chinese Academy of Sciences, Beijing 100190, People's Republic of China*

(Received 2 November 2021; revised 12 January 2022; accepted 24 February 2022; published 8 March 2022)

Pressure not only provides a powerful way to tune the crystal structure of transition-metal dichalcogenides (TMDCs) but also promotes the discovery of exotic electronic states and intriguing phenomena. Structural transitions from the quasi-two-dimensional layered orthorhombic phase to three-dimensional cubic pyrite phase, metallization, and superconductivity under high pressure have been observed experimentally in TMDC materials PdS_2 and $PdSe_2$. We report a theoretical prediction of the pressure-induced evolutions of crystal structure and electronic structure of PdSSe, an isomorphous intermediate material of the orthorhombic PdS_2 and $PdSe_2$. A series of pressure-induced structural phase transitions from the layered orthorhombic structure into an intermediate phase and then to a cubic phase is revealed. The intermediate phase features the same structure symmetry as the ambient orthorhombic phase, except for drastic collapsed interlayer distances and striking changes of the coordination polyhedron. Furthermore, the structural phase transitions are accompanied by electronic structure variations from semiconductor to semimetal, which are attributed to bandwidth broadening and orbital-selective mechanisms. Specifically, the cubic phase PdSSe is distinct from the cubic PdS_2 and $PdSe_2$ materials by breaking inversion and mirror-plane symmetries but showing similar superconductivity under high pressure, which originates from strong electron-phonon coupling interactions concomitant with topologically nontrivial Weyl and high-fold fermions. The intricate interplay between lattice, charge, and orbital degrees of freedom as well as the topologically nontrivial states in these compounds will further stimulate wide interest to explore the exotic physics of the TMDC materials.

DOI: 10.1103/PhysRevB.105.115110

I. INTRODUCTION

Since the discovery of atomic thin graphene, two-dimensional (2D) materials have received extensive attention [1,2]. As one important branch of 2D materials, transition-metal dichalcogenide (TMDC) materials have attracted more and more interest due to their superior electronic, optical, mechanical, and catalytic properties [3]. Layered TMDC materials MX_2 are commonly composed of quasi-2D X-M-X–type sandwich layers held together by weak van der Waals (vdW) forces, in which M is the transition-metal element and X is the chalcogen element such as S, Se, or Te. The bulk-phase MX_2 often crystallizes in the $1T$ polytype consisting of monolayer MX_6 octahedra, and the $2H$ and $3R$ polytypes with bilayer and trilayer stacked trigonal prismatic coordinated MX_6 layers [4]. As new members of the TMDC family, the noble-metal dichalcogenides (NMDCs) PdX_2 materials are potential candidates for exotic physical properties and novel technical applications at the nanoscale [5–7]. Among them, $PdTe_2$ tends to crystallize in a $1T$ structure with octahedral coordination [8,9], whereas PdS_2 and $PdSe_2$ adopt an unconventionally orthorhombic structure named the $2O$ phase at ambient conditions, in which each Pd atom coordinates with four chalcogen atoms in a $(PdX_4)^{2-}$ square plane and resulting in a puckered pentagonal morphology [10,11]. Due to the strange pentagonal structure and unusual interlayer coupling interactions [12], the $2O$ phase PdS_2 and $PdSe_2$ materials host excellent physical-chemical properties and promising application prospects [5–7], including layer-dependent tunable band gaps [13–17], highly anisotropic properties [18–27], and ultrahigh air stability [17], which are promising materials for field-effect transistor [18,24], broadband photodetector [19,28,29], thermoelectric applications [13,21–23] and nonlinear photoelectronic devices [30].

Similar to conventional 2D semiconductors, the physical properties of PdS_2 and $PdSe_2$ are susceptible to external perturbations such as light [30], electric field [31], molecular adsorption [32], applied pressure [33–37], and strain [25,27,35,38–41]. Particularly, pressure and strain are two

*Corresponding author: mingxing@glut.edu.cn

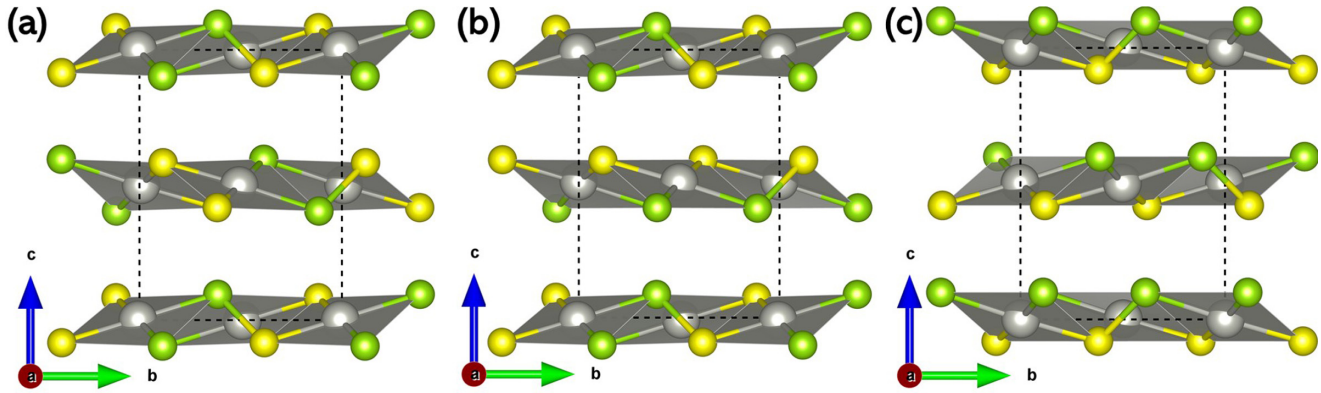

FIG. 1. Three polymorphs of PdSSe in (a) *AA*, (b) *AB*, and (c) *BB* stacking manner with gradually increasing energy. The big gray balls represent Pd atoms, while the small yellow (green) balls represent S (Se) atoms.

effective means to tailor the crystal structures and electronic structures of PdS_2 and $PdSe_2$. PdS_2 and $PdSe_2$ undergo structural transitions from the layered $2O$ phase to cubic pyrite-type structure under pressure, accompanied by metallization and superconductivity [33–36]. Theoretical investigations propose that the metallic electron structure originates from an orbital-selective mechanism [33,35]. High-pressure experiments reveal a dome-shaped relationship of the superconducting temperature with the pressure for the cubic pyrite phase PdS_2 and $PdSe_2$ [33,36]. Electronic structure calculations indicate that the superconductivity originates from strong electron-phonon coupling interactions combined with topological nodal-line states [35,36]. Meanwhile, excellent ferroelasticity with a low energy barrier and strong switching signal under strain has been theoretically predicted for PdS_2 and $PdSe_2$, with great potential for the application of shape memory devices [25,27,35,38]. Furthermore, these ferroelastic transitions accompanied with crystal orientation rotations give rise to tunable transport properties and switchable thermal conductivity [25,27,35,40].

Not only external stimuli but also internal factors such as vacancy defects [16,42–45], chemical doping [46–48], and surface oxidation [49] can be utilized to trigger structural transitions and manipulate the physical-chemical properties of PdS_2 and $PdSe_2$. Experiments demonstrate that plasma irradiation [42] or electron irradiation [44] can induce Se atom vacancy in $PdSe_2$, which breaks the Se-Se dumbbell-shaped dimers and results in huge structural distortions and formation of metallic $Pd_{17}Se_{15}$ and novel 2D Pd_2Se_3 materials [42,44]. The defect states in $PdSe_2$ can be reversibly switched between charge neutral and charge negative and show anisotropic carrier mobility [43,45]. First-principles theoretical investigations show that hole doping can induce half-metallic ferromagnetism in the $PdSe_2$ monolayer, and the magnetization direction can be controlled by a transverse uniaxial stress [48]. Furthermore, controllable partial oxidation of the surface of $PdSe_2$ by ozone treatment successfully modifies its transport property, optoelectronic performance, and catalytic activity [49]. On the other hand, due to the different ionic radii, doping or substitution can induce chemical pressure in crystals, which are considered as specific methods conducive to stabilizing pressure-induced superconductivity or other characteristic phenomena at ambient conditions [50]. Recently, Te substitution-induced structural evolutions from the orthorhombic $2O$ phase to a monoclinic verbeekite phase and then to a trigonal $1T$ phase are observed in the $PdSe_{2-x}Te_x$ system, accompanied by a drastic change of the electrical transport behavior from semiconductor to metal and enhanced superconductivity with increasing Te content [46,51]. In addition, a solid solution of $PdSe_{2-x}S_x$ with a wide range of x ($0 \leqslant x \leqslant 0.86$) has been synthesized by atomic substitution, which shows tunable density of states, effective mass, and band gap by changing x [47].

Although $2O$-phase PdSSe, an isomorphous intermediate material of orthorhombic PdS_2 and $PdSe_2$, has been synthesized for over half a century [11], its detailed crystal structure is only reported by our theoretical works recently [52]. As shown in Fig. 1, the bulk phase of PdSSe is constituted by two types of monolayer PdSSe (denoted as *A* and *B*) and forms three polymorphs with different stacking manners (denoted as *AA*, *AB*, and *BB*). Previous theoretical predictions indicate that PdSSe will exhibit intriguing properties, including excellent photocatalytic properties and tunable band gap under biaxial strain, which are promising characteristics for high-performance optoelectronic, nanoelectronic, photovoltaic, and photocatalytic applications [52,53]. Although tremendous focus has been paid to PdS_2 and $PdSe_2$, the study on their counterpart PdSSe is scarce. Considering that PdS_2 and $PdSe_2$ are featured with rich phase transitions, tunable properties, and interesting superconducting behavior under stress or pressure [25,27,33–41], one may naturally expect similar behavior to be observed in their sister material PdSSe. In the present work we explored the structural evolutions of the bulk-phase PdSSe under hydrostatic pressure, uncovered an electronic structure transition from semiconductor to semimetal and superconductor, revealed the origin of the metallization, and predicted topological superconductivity for the high-pressure phase. The predicted structural transitions and unconventional transport properties concomitant with topologically nontrivial states in PdSSe supply a meaningful complement to the hectic NMDC materials of PdS_2 and $PdSe_2$, which will attract extensive interest from a wide audience to explore its unanticipated properties.

II. CALCULATION METHODS

Geometry optimization and electronic structure calculations were performed by using the Vienna *Ab initio* Simulation Package (VASP) [54,55] based on the density functional theory. The projector-augmented-wave potential, the Perdew-Burke-Ernzerhof (PBE) exchange-correlation functional [56], and the plane-wave basis set with a cut-off energy of 520 eV were employed. The smallest allowed spacing of the reciprocal space between k points was fixed to 0.2 Å^{-1}. In order to obtain a more accurate band gap close to the experimental value, the Heyd-Scuseria-Ernzerhof (HSE06) [57,58] hybrid density functional was adopted to calculate the band structures. Electron-phonon interaction calculations were performed by the density functional perturbation theory with the QUANTUM ESPRESSO (QE) code [59]. Electron-phonon coupling constants were calculated on phonon and electron grids of $4 \times 4 \times 4$ and $16 \times 16 \times 16$, respectively, with a Gaussian smearing width of 0.05 Ry, and the plane-wave cut-off energy was set to 50 Ry for all three polymorphs of PdSSe. As shown in Fig. S1 in the Supplemental Material (SM) [60], the convergence tests of energy cutoff and sampling of k points demonstrated the parameters employed in the present work were convincing and accurate enough.

The electron-phonon coupling constant λ and the superconducting transition temperature T_c for PdSSe are calculated by the Allen-Dynes-modified McMillan formula [61,62]:

$$T_c = \frac{\omega_{\log}}{1.2} \exp\left[-\frac{1.04(1+\lambda)}{\lambda - \mu^* - 0.62\lambda\mu^*}\right], \quad (1)$$

where the Coulomb pseudopotential μ^* is set to 0.1, and the electron-phonon coupling constant λ is defined as

$$\lambda = 2\int_0^\infty \frac{\alpha^2 F(\omega)}{\omega} d\omega, \quad (2)$$

and $\omega_{\log}$ is the logarithmic average frequency,

$$\omega_{\log} = \exp\left[\frac{2}{\lambda}\int \frac{\log \omega}{\omega}\alpha^2 F(\omega) d\omega\right], \quad (3)$$

where $\alpha^2 F(\omega)$ is the Eliashberg spectral function, defined as

$$\alpha^2 F(\omega) = \frac{1}{2\pi N(E_f)} \sum_q \delta(\omega - \omega_q)\frac{\gamma_q}{\hbar\omega_q}, \quad (4)$$

where $N(E_f)$ is the density of states (DOS) at the Fermi level and γ_q is the phonon linewidth.

It is very important to include vdW correction methods to describe the interlayer spacing and the out-of-plane lattice constant c of the quasi-2D layered materials [63]. Due to the lack of a detailed crystal structure of PdSSe, the choice of vdW scheme was based on its sister compounds PdS_2 and $PdSe_2$ in our previous work [52]. In the present work, further screening was carried out. As shown in Table S1 in the SM [60], without considering the vdW corrections, the standard local-density approximation (LDA) functional excessively underestimates the lattice constant c, while the PBE functional extremely overestimate the lattice constant c. Therefore, the density-dependent energy correction (dDsC) [64,65] was adopted to consider the interlayer vdW interactions. As shown in Table I, the theoretically optimized lattice constants calculated by PBE together with dDsC (hereafter denoted as PBE+dDsC and used for all calculations within VASP, unless otherwise stated) are closer to the experimental value than our previous results (Table I in Ref. [52]), demonstrating the validity of the calculation parameters. Additionally, the energies are comparable with each other for these three polymorphs of PdSSe, and they show a similar structural phase transition and high-pressure superconductivity. Therefore we mainly presented the results and discussions of the *AA* polymorph of PdSSe in the main text, and the results for the other two polymorphs (*AB* and *BB*) were provided in the SM [60].

TABLE I. The optimized lattice constants, unit-cell volume (V_0), and relative energy E_r of the three most stable polymorphs of bulk-phase PdSSe compared with the experimental results.

	a (Å)	b (Å)	c (Å)	V_0(Å^3)	E_r (meV/atom)
Expt [11].	5.595	5.713	7.672	245.23	–
AA	5.628	5.742	7.663	247.665	0.00
AB	5.631	5.740	7.664	247.718	1.60
BB	5.639	5.743	7.625	246.951	1.79

III. RESULTS AND DISCUSSION

A. Structural evolution under hydrostatic pressure

The structural evolution under compression has been simulated by gradually increasing the pressure from 0 to 10 GPa. As shown in Fig. 2(a), the lattice constants show an anisotropic response to the hydrostatic pressure. Attributed to the weak interlayer connection of vdW bonds, the out-of-plane lattice constant c significantly shrinks when pressure increases to 3 GPa. In contrast, the lattice constants a and b increase slowly. The vdW radii of Pd, S, and Se ions are 2.15, 1.8, and 1.9 Å, whereas the covalent radii of Pd, S, and Se ions are 1.39, 1.05, and 1.20 Å [66,67]. Apparently, the interlayer and intralayer Pd-X bonds belong to vdW and covalent bonds, respectively. Compared with the easily compressed interlayer vdW bonds along the stacking direction, the in-plane intralayer covalent bonds in the $(Pd{-}S_2{-}Se_2)^{2-}$ square plane are less affected by applied pressure [Fig. 2(b)]. At a pressure of 3.5 GPa, the orthorhombic PdSSe transforms to an intermediate phase. The intermediate phase still has the identical crystallographic symmetry with the ambient-pressure phase, but the out-of-plane lattice constants c dramatically shrink accompanied by obvious expansions of the in-plane lattice constants a and b. Meanwhile, the interlayer Pd-X distances between Pd atoms and chalcogen atoms X in the adjacent layer decrease sharply, being close to the intralayer counterparts. This drastic structural change causes a sudden volume collapse [Fig. 2(c)] and energy increase [Fig. 2(d)]. All the lattice constants become equal, and the orthorhombic PdSSe transforms to a cubic phase above 4 GPa (the structure symmetry will discussed later in Sec. II C). Furthermore, three distinct stages of structural transition in the isostructural and isoelectronic PdS_2 and $PdSe_2$ have been observed by high-pressure experiments, and the 2O orthorhombic phase has been proposed to coexist with the cubic pyrite phase in the intermediate stage [33,34,36]. Regretfully, there are no

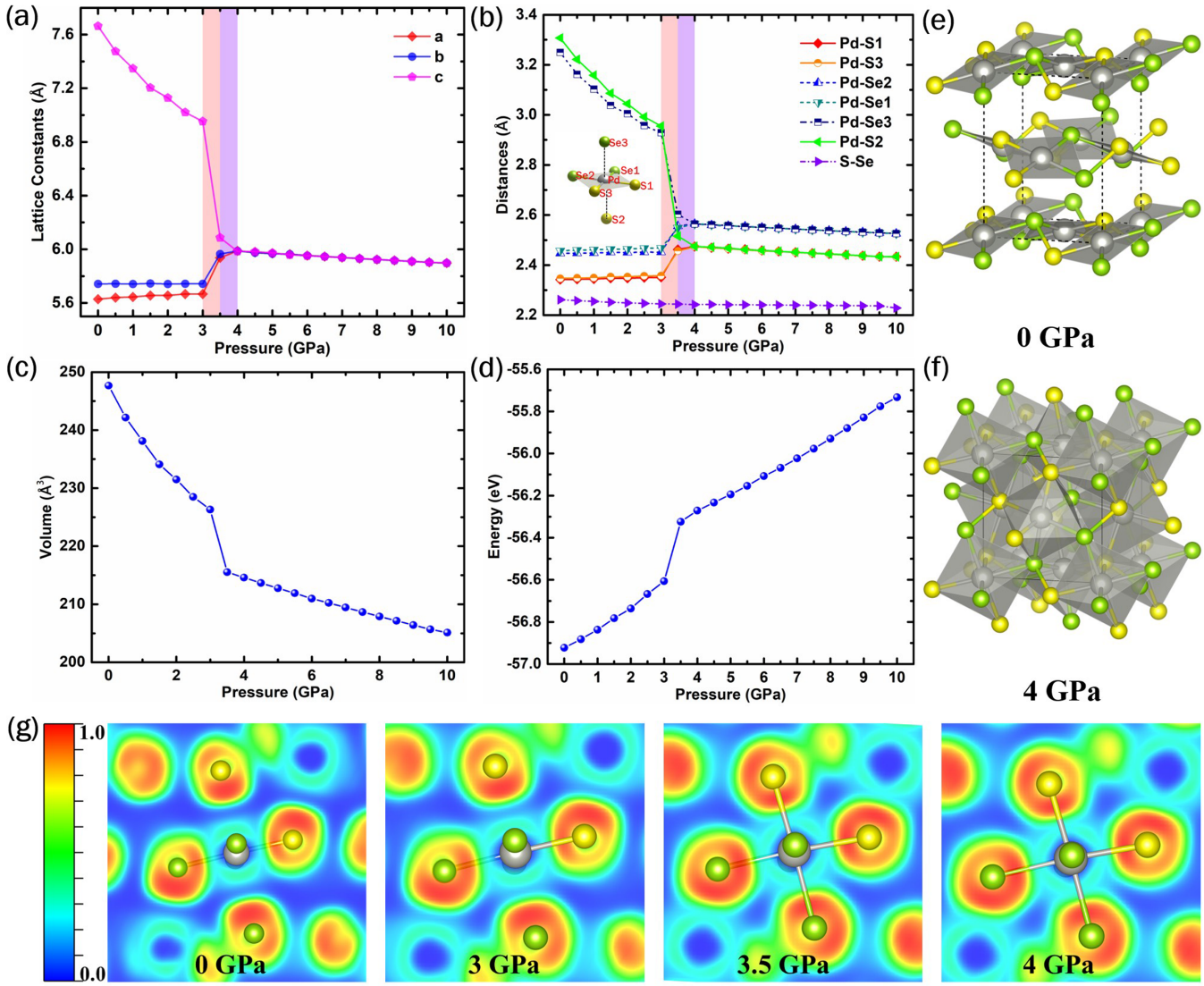

FIG. 2. Evolutions of crystal structure and electronic structure of PdSSe under hydrostatic pressure: (a) lattice constants, (b) interatomic distances (the inset illustrates the coordination environment of the Pd atom), (c) volume, and (d) energy changes as a function of pressure and crystal structure with coordination polyhedra at (e) 0 GPa, (f) 4 GPa, and (g) slices of the electron localization function at different pressures.

experimental studies on PdSSe crystals under pressure to date. Therefore we have to employ the lattice constants at the ambient condition as a starting point and the sister materials PdS_2 and $PdSe_2$ as references. In addition, we have also checked the structural evolution under pressure with standard PBE and LDA functionals (without considering the vdW corrections). As shown in Fig. S2 in the SM [60], compared to the experimental reported lattice parameters and the transition pressure predicted by PBE+dDsC, LDA underestimates the lattice constant c and the transition pressure, whereas PBE overestimates the lattice constant c and the transition pressure. Overall, our theoretical calculations indicate that PdSSe will undergo structural transformation under compression and an intermediate phase may exist during the transition process, which implies that a coexisting region of the orthorhombic phase with the cubic phase may be observed in PdSSe by future high-pressure experiments.

According to the pressure homology principle, the origin of the pressure-induced structural transition of PdSSe from the $2O$ orthorhombic phase to the cubic phase can be explained by the displacive mechanism [34]. In fact, the layered orthorhombic phase is derived from a structural distortion of the cubic phase, and the unusual $(Pd{-}S_2{-}Se_2)^{2-}$ square-planar coordination originates from the elongation octahedron along the out-of-plane direction [33,35]. The elongation of the octahedron belongs to the Jahn-Teller (JT) distortion, which is attributed to the degeneracy of the d-electron state. The JT distortion degree is estimated by a distortive degree parameter $\Delta_d = 1/6 \sum_{i=1}^{6} [(R_i - \bar{R})/\bar{R}]^2$, where R_i and $\bar{R}$ denote individual and average values of the Pd-X bonds, respectively [68]. The out-of-plane chalcogen X ions gradually approach the coordinated central Pd ions with apparent displacements, which leads to a rapid decrease of the distortive degree (Δ_d) as a function of pressure below 3 GPa (as shown in Fig. S3 [60]). The interlayer Pd-X distances are about 3.3 (Pd-S)

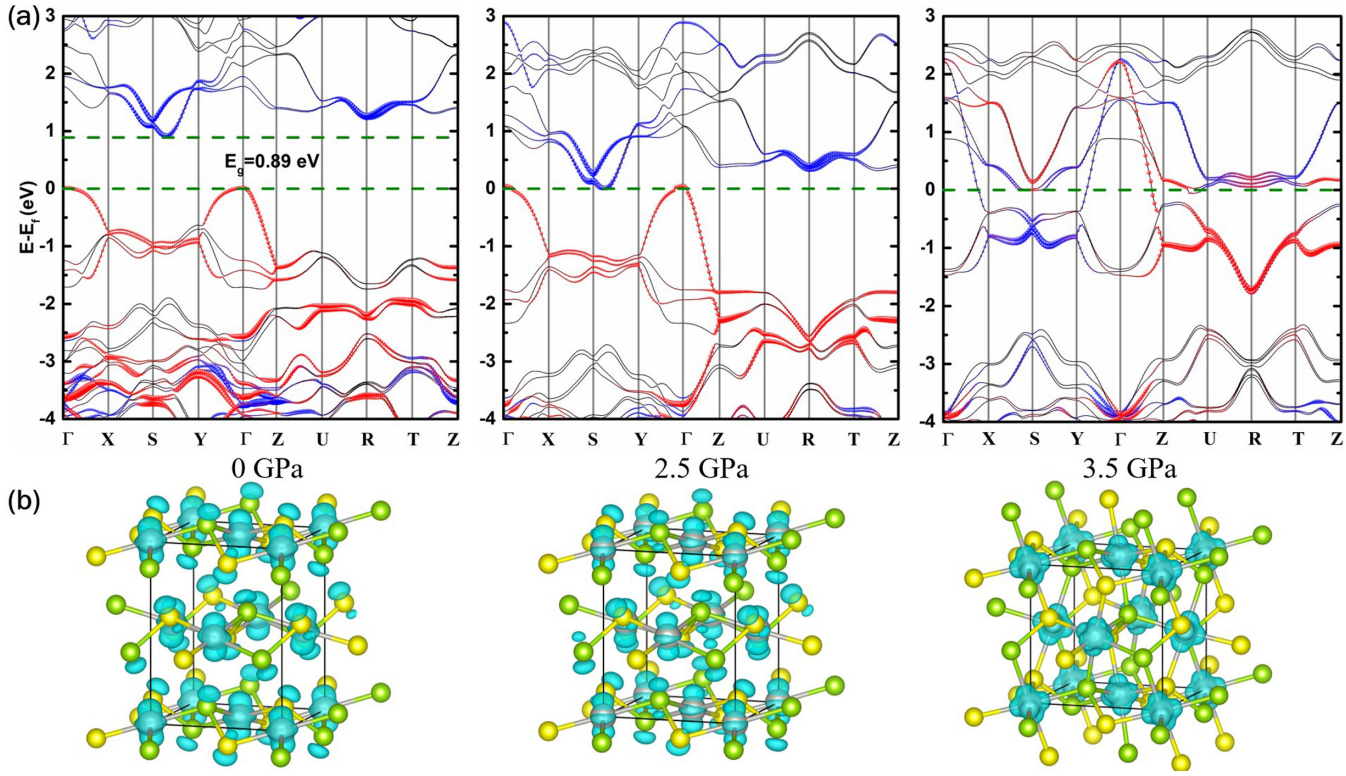

FIG. 3. The electronic structure of PdSSe under different hydrostatic pressures: (a) band structures calculated by HSE06. The contributions of the $d_{x^2-y^2}$ (blue balls) and d_{z^2} (red balls) orbitals are proportional to the size of the colored balls. (b) The corresponding partial charge density. The selected energy range of the bands that are used for the evaluation of the partial charge density is set to −1 to 0 eV.

and 3.2 (Pd-Se) Å at ambient conditions, which are on the verge of the vdW bond (3.1 ∼ 5.0 Å) [35]. The interlayer Pd-X distances shrink quickly along with compression and go below the threshold value of vdW interactions when the pressure increases up to 3 GPa. Further compression leads to the collapse of interlayer spacing and the annihilation of vdW interactions. Consequently, the distortive degree (Δ_d) of the PdX_6 octahedron is sharply suppressed at 3.5 GPa, and the orthorhombic lattice changes to a cubic one when pressure increases up to 4 GPa. Meanwhile, the coordination polyhedron transforms from a square plane into an almost normal octahedron [Figs. 2(e) and 2(f)], as demonstrated by the tiny Δ_d in Fig. S3 [60]. The electron localization function (ELF) reveals the changes of the interlayer bonding interactions [Fig. 2(g)]. Ranging from 0 to 3 GPa, the ELF is almost zero in the interlayer spacing, where no covalent bond exists. Above 3.5 GPa, the interlayer charge density significantly increases, and a covalent interaction gradually emerges between the metal Pd and the chalcogen X ions in the adjacent layer. The dynamic stability of the cubic phase at 4 GPa is examined by the phonon spectrum. As shown in Fig. S4 [60], the phonon spectrum calculated by the PBE+dDsC and PBE exchange-correlation functional shows evident imaginary frequencies at the Γ point, which can be nearly eliminated by switching to the LDA functional, indicating that such imaginary frequencies are probably not caused by structural instability (a phenomenon which also exists in the monolayer $PdSe_2$ [17]). Therefore the compression almost eliminates the JT distortion in PdSSe and renders the cubic structure stable under high pressure. Recent experiments have shown that $PdSe_2$ underwent a structural transformation from layered orthorhombic phase to cubic pyrite-type structure at 6 ∼ 10 GPa [34,36], while a similar structural transition occurs at a pressure of 16 GPa for its isostructural compound PdS_2 [33]. Our previous theoretical studies have confirmed the emergence of a stable cubic pyrite structure when the JT distortive degree of PdS_2 was absolutely eliminated by pressure [35], whereas the distortive degree of cubic-phase PdSSe still retains a certain value due to the different ionic radii of S and Se. Anyway, we can still expect that structural transformations from the layered orthorhombic phase to cubic phase will be realized in PdSSe by high-pressure experiments according to the pressure homology principle [33–36].

B. Electronic structure transitions from semiconductor to semimetal under compression

The pressure-induced structural transition is also accompanied by electronic structure variations. Like many semiconducting TMDC materials [69], as the interlayer distances decrease during compression, the band gaps of PdSSe gradually decrease until complete closure (Fig. S5 [60]). Under ambient pressure, the band structures of all three polymorphs PdSSe show indirect semiconducting characteristics [52]. The calculated band gaps of ∼0.89 eV are slightly larger than the experimental value of 0.65 eV [11], which may be due to the overestimation of the HSE06 functional (Fig. 3). In addition, due to the elongated lattice constants in the c direction, the calculated band gaps in the present paper are slightly larger than those of our previous work (0.62 ∼ 0.78 eV) [52].

This phenomenon indicates that the band gap of PdSSe is extremely sensitive to the interlayer distance, similar to the case of $PdSe_2$ [17]. The band gap of PdSSe closes up at 2.5 GPa. As shown in Fig. 3(a), the band dispersion at 2.5 GPa is very similar to that at 0 GPa, but the valence band maximum (VBM) is higher than the conduction band minimum (CBM), displaying a typical characteristic of semimetal. Further increasing pressure up to 3.5 GPa leads to the lattice transform to an intermediate phase with collapsed interlayer spacing. Though the orthorhombic symmetry remains unchanged, the interlayer interactions are dominant by the covalent bond rather than vdW forces. The collapsed interlayer spacing gives rise to a nearly metallic band structure for the intermediate phase. In fact, there are obvious charge gaps between the valence bands and conduction bands along most parts of the high-symmetric paths [right column of Fig. 3(a)], while they only nearly contact with each other along the high-symmetric paths of Γ-X, Γ-Y, and Γ-Z (see a zoom-in picture of the band structure at 3.5 GPa in Fig. S6 [60]). Therefore the pressure-induced intermediate phase of PdSSe can be still viewed as semimetal.

Previous resistivity experiments observed semiconductor-to-metal transitions in PdS_2 ($PdSe_2$) at 7 (3) GPa [33,36]. However, the pressure-induced metallization in PdS_2 and $PdSe_2$ occurs before the structural transition to the cubic phase. Therefore the metallization of the intermediate phase in PdS_2 and $PdSe_2$ is not related to the cubic structure but originated from the broadening of the energy bands and filling-changes of the Pd-d orbitals around the Fermi level [33,35]. We propose that the pressure-induced metallization in PdSSe can also be explained by an orbital-selective mechanism. As shown in Fig. 3, the distributions of the Pd 4d orbital near Fermi energy are obviously changed under pressure, consistent with the variation of the coordination environments of the Pd atoms. Before the structure changing to the intermediate phase, the $d_{x^2-y^2}$ and d_{z^2} orbitals are separated from each other and dominant to the CBM and VBM, respectively [35]. The electronic structural transition from semiconductor to semimetal originates from the bandwidth broadening [middle column of Fig. 3(a)], which can be completely attributed to the increase of the hopping due to the reduced interlayer distance. When the lattice collapses into the intermediate phase, the coordination polyhedron of Pd ion changes from square plane to distorted octahedron. Accordingly, the corresponding energy of the d_{z^2} orbital increases, which results in a reduction of the crystal-field splitting between $d_{x^2-y^2}$ and d_{z^2} orbitals. Mixed-filled $d_{x^2-y^2}$ and d_{z^2} orbitals obviously contribute to the bands around the Fermi level [right column of Fig. 3(a)], implying the orbital-selective mechanism is responsible for the metallization [33,35].

The metallization process can be further inspected by the variation of the band structure combined with local charge density analysis. As shown in Fig. 3(b), we can see obvious variations of the occupied orbital along with the increasing pressure. Similar to PdS_2 and $PdSe_2$, the Pd ion has a nominal $+2$ valence state with $4d^8$ electron configuration in PdSSe. At ambient-pressure conditions, the 4d electrons of Pd^{2+} preferentially occupy lower energy d_{xz}, d_{yz}, d_{xy}, and d_{z^2} orbitals according to the square-planar crystal-field splitting [70]. Therefore the empty $d_{x^2-y^2}$ orbitals locate above the Fermi level and are separated from the occupied d_{z^2} orbitals by a charge gap. In addition, the dispersions of the VBM along Γ-X and Γ-Y directions are highly similar at ambient pressure, which are weaker than the highly dispersive bands along Γ-Z direction (left column of Fig. 3), suggesting a strong interlayer coupling interaction [12]. Upon compression, the chalcogen ions X from the adjacent layers get closer to the central Pd atom, resulting in a distorted octahedral coordination. The uppermost valence bands are broadened along with increasing pressure, and the gradually increasing energy of d_{z^2} orbital leads to a shrinkage of the energy gap between the $d_{x^2-y^2}$ and d_{z^2} orbitals, resulting in a semiconductor-to-semimetal transition (middle column of Fig. 3). Further increasing the pressure, the distortive degree of octahedra is almost annihilated after the collapse of the interlayer spacing (Fig. S3 [60]), and then the interlayer covalent bonds are established. The reductions of crystal-field splitting between $d_{x^2-y^2}$ and d_{z^2} orbitals cause a mixture of the empty $d_{x^2-y^2}$ orbitals with the filled d_{z^2} orbitals, which forms doubly degenerate e_g states ($d_{x^2-y^2}$ and d_{z^2}). At 3.5 GPa, the triply degenerate full-filled t_{2g} states (d_{xy}, d_{xz}, and d_{yz}) form localized narrow bands at the lower energy region, which are separated from the half-filled e_g states ($d_{x^2-y^2}$ and d_{z^2}) by a big gap of $\sim$0.57 eV comparable to the counterpart in PdS_2 (0.7 eV) [35]. The half-filled e_g states show similar dispersion characteristics along Γ-X, Γ-Y, and Γ-Z directions (Fig. S6 [60]). Especially, the bands crossing the Fermi level along Γ-X and Γ-Y directions are mainly contributed from the $d_{x^2-y^2}$ orbitals, in contrast to the d_{z^2} orbitals along the Γ-Z direction, which results in a semimetallic band structure in the intermediate phase (right column of Fig. 3(a) and Fig. S6 [60]). Finally, the intermediate phase transforms into the cubic phase upon pressure increasing to 4 GPa, whose transport properties under high pressure will be discussed in the next section.

C. Topological superconductivity of the high-pressure cubic phase

More interestingly, previous experiments demonstrate that the high-pressure cubic phase PdS_2 and $PdSe_2$ show superconductivity and display dome-shaped superconducting diagrams [33,36]. Electron structure analysis of the cubic phase PdS_2 and $PdSe_2$ indicates that the superconductivity under high pressure is related to the Dirac states and nodal-line states near the Fermi level [35,36]. As shown in detail in Fig. 4, the band structure of the high-pressure cubic phase PdSSe highly resembles those of the cubic superconducting PdS_2 and $PdSe_2$. The bands crossing the Fermi level exhibit excellent metallicity with strong hybridization between the S 3p, Se 4p states and Pd 4d states, as demonstrated by the projected band structure in Fig. S7(a) [60]. The parabolic bands around the Fermi level at the Γ point are considered to be associated with strong electron-phonon coupling and conventional superconductivity. Therefore we speculate that the transport properties of PdSSe are qualitatively similar to the superconductivity of PdS_2 and $PdSe_2$ under high pressure.

However, in contrast to the eightfold degeneracies (considering the spin degeneracy) of the energy bands at the M point for the PdS_2 and $PdSe_2$, energy bands of PdSSe at

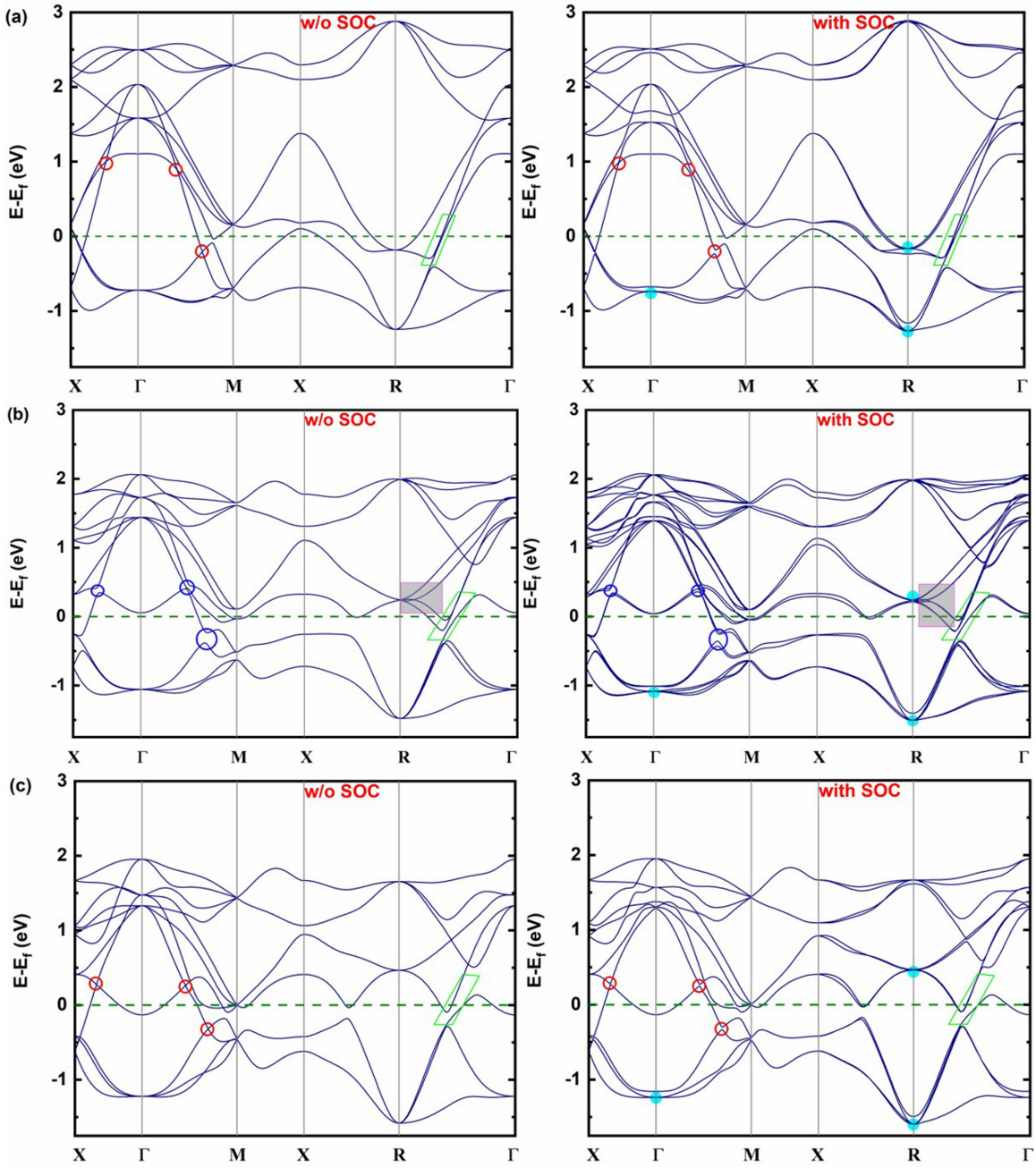

FIG. 4. Comparisons of the band structure of the cubic-phase (a) PdS_2, (b) PdSSe (*AA* polymorph), and (c) $PdSe_2$ at pressure of 4 GPa without (w/o) or with SOC interactions. The green rhombus illustrates the charge gap along the Γ-*R* directions. The Dirac and nodal-line states are marked by the red circles in (a) and (c), while they are broken as indicated by the blue circles in (b). The cyan points mark the fourfold and sixfold degenerate fermions at the Γ point and *R* point. The Weyl points along the Γ-*R* line are highlighted by the shadow rectangles in (b), which are enlarged as shown in Fig. S8 [60].

the *M* point split into pairs of fourfold degenerate bands. In addition, the inversion symmetry breaking furher lifts the degeneracies of the band structure along the high-symmetric directions when the spin-orbit coupling (SOC) interactions are taken into account. Specifically, the Dirac states and nodal-line states protected by the glide mirror symmetry of the space group $Pa\bar{3}$ in PdS_2 and $PdSe_2$ are broken in PdSSe. These significant changes of the band structure originate from the absence of inversion and mirror-plane symmetries in PdSSe with respect to those of the cubic pyrite-type PdS_2 and $PdSe_2$. Therefore, strictly speaking, the structure symmetry (no. 198 space group $P2_13$) of the high-pressure phase PdSSe (*AA* polymorph) belongs to the cubic ullmannite-type structure rather than the cubic pyrite-type structure with the no. 205 space group $Pa\bar{3}$ [71]. As shown in Fig. 4, the twofold screw rotation ($\tilde{c}_{2\alpha}$) and threefold rotation (C_3) symmetries of the nonsymmorphic cubic space groups (no. 198 and no. 205) give rise to exotic fourfold and sixfold degenerate fermions at the Γ point and *R* point, respectively [72,73]. Particularly, the lowest conduction band and the highest valence bands

along high-symmetry lines are completely gapped out after considering the SOC interactions for PdSSe, PdS_2, and $PdSe_2$, demonstrating typical characteristics of topological semimetal for these compounds and providing a possible venue for the emergence of nontrivial surface states. We carry out a trial calculation of the symmetry-based indicator and receive a $Z_4 = 1$ for both the cubic pyrite-type PdS_2 and $PdSe_2$ (no. 205 space group $Pa\bar{3}$) [74–77], which indicates strongly topological properties awaiting further detailed investigation. Furthermore, Weyl fermions can arise in the cubic phase PdSSe due to the breaking of inversion symmetry, as demonstrated by the Weyl points along the Γ-*R* line [Fig. 4(b)] induced by the crossing of bands with different C_3 eigenvalues [72]. (A close view of the band crossing points near the high-symmetric *R* point around the Fermi level is presented in Fig. S8 [60].) The superconductivity seems to be intertwined with these topologically nontrivial states [78].

As shown in Fig. S7(b) [60], the Fermi surface of PdSSe consists of a large cubelike pocket at the center of the Brillouin zone and a network of small electron and hole pockets connected along the edges of the Brillouin zone, which are consistent with the multifold degeneracies. The cubelike Fermi surface with small curvature indicates that the cubic-phase PdS_2 and PdSSe are likely to produce quantum oscillations with large effective mass [35,79,80]. Furthermore, the nontrivial topological states close to the Fermi level contribute considerable DOS values at the Fermi level for the high-pressure phase (Fig. S9) [60], which combined with the large Fermi surface may provide sufficient channels for electron-phonon scattering [81] and favor an enhancement of the electron-phonon interaction [82]. Therefore since the cubic phase PdSSe features similar dispersion characteristics of the band structure, topological states, and Fermi surface with the superconducting phase PdS_2 and $PdSe_2$, we expect similar superconducting behaviors will be observed in PdSSe by high-pressure experiments.

In order to confirm the possible superconductivity in cubic-phase PdSSe under high pressure, we calculate the electron-phonon coupling constant λ and the superconducting transition temperature T_c for PdSSe. Correspondingly, the phonon DOS (PhDOS) displays three regions separated by two gaps (Fig. 5). The heaviest Pd atoms predominantly contribute to the low-frequency acoustic branches, while the lighter Se atoms contribute to the middle-frequency optical branches. The contributions of the lightest S atoms are very tiny in the low- and middle-frequency region, and predominantly dominate the high-frequency optical branches. The broad distribution of electron-phonon interactions is reflected in the calculated Eliashberg spectral function $\alpha^2F(\omega)$ [83]. Calculated results show that there are strong electron-phonon interactions in the pressure-induced cubic phase PdSSe. The electron-phonon coupling constant λ of the cubic phase PdSSe at 4 GPa is 0.75, and the corresponding superconducting transition temperature T_c is 7.5 K. Therefore the theoretically calculated T_c of cubic-phase PdSSe at 4 GPa is comparable to the theoretical calculated T_c of 4.9 (7.6) K for the cubic pyrite phase PdS_2 ($PdSe_2$) at 4 (10) GPa [35]. Furthermore, the experimental observed T_c of the cubic pyrite phase PdS_2 and $PdSe_2$ shows dome-shaped dependence on pressure, which increases up to maximum values of 8.0 and 13.1 K at 37.4 and 23 GPa, respectively [33,36]. We further examine the stability and superconductivity of the cubic-phase PdSSe under pressure. As shown in Fig. S10 [60], the phonon spectra without any imaginary frequencies indicates that the cubic PdSSe can be dynamically stable at 0 GPa. The corresponding PhDOS almost display identical characteristics to that at 4 GPa. The calculated electron-phonon coupling constant λ is 0.68 and the corresponding superconducting transition temperature T_c is 5.8 K, which increases along with the increasing pressure. The increasing trend of the theoretically calculated superconducting temperature from 5.8 K (at 0 GPa) to 7.5 K (at 4 GPa) to 10.1 K (at 10 GPa) is in line with the experimental observations [33,36] and the theoretical calculated results [35] for cubic-phase PdS_2 and $PdSe_2$ (Fig. 6). Therefore the pressure-induced evolutions of the crystal structure and electronic transport properties of PdSSe are qualitatively similar to those of PdS_2 and $PdSe_2$. The experiments revealed a dome-shaped relationship of the superconducting temperature with the pressure for the high-pressure cubic phase PdS_2 ($PdSe_2$), which can increase up to maximum values of 8.0 (13.1) K at 37.4 (23) GPa, respectively. As shown in Fig. 6(b), the T_c of PdSSe is higher than the counterparts of PdS_2 and $PdSe_2$ at the studied pressure range, and we can expect it to increase to much higher values by further compression.

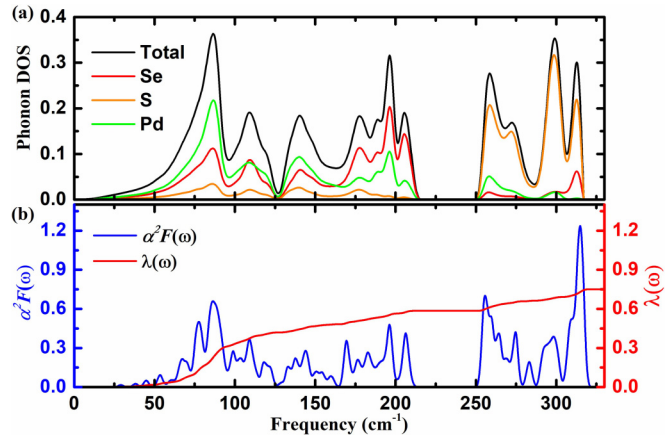

FIG. 5. Calculated (a) phonon density of states (PhDOS) and (b) Eliashberg electron-phonon coupling spectral function $\alpha^2F(\omega)$ and the electron-phonon coupling integral $\lambda(\omega)$ of cubic PdSSe at 4 GPa.

Previous experiments indicate that the superconductivity shows a striking correlation with the structural instability of the chalcogen dumbbells in cubic pyrite phase $PdSe_2$ [36]. However, despite showing similar Se-Se bond softening under pressure, the isostructural and isoelectronic pyrite phase $NiSe_2$ remains nonsuperconducting up to 50 GPa [33]. Moreover, high-pressure Raman spectroscopy and theoretical calculations do not observe any anomalous softening of the S-S bonding in the isomorphous cubic pyrite phase PdS_2 [33,35]. The symmetric chalcogen Se-Se (S-S) dumbbells in the cubic $PdSe_2$ (PdS_2) have been broken and replaced by the S-Se bond in the cubic phase PdSSe. And our theoretical calculations reveal that the S-Se bond lengths in cubic phase PdSSe are nearly independent of pressure [Fig. 2(b)], similar to the rigid S-S bond observed in the cubic pyrite phase PdS_2. Therefore the structural instability of the chalcogen dumbbells

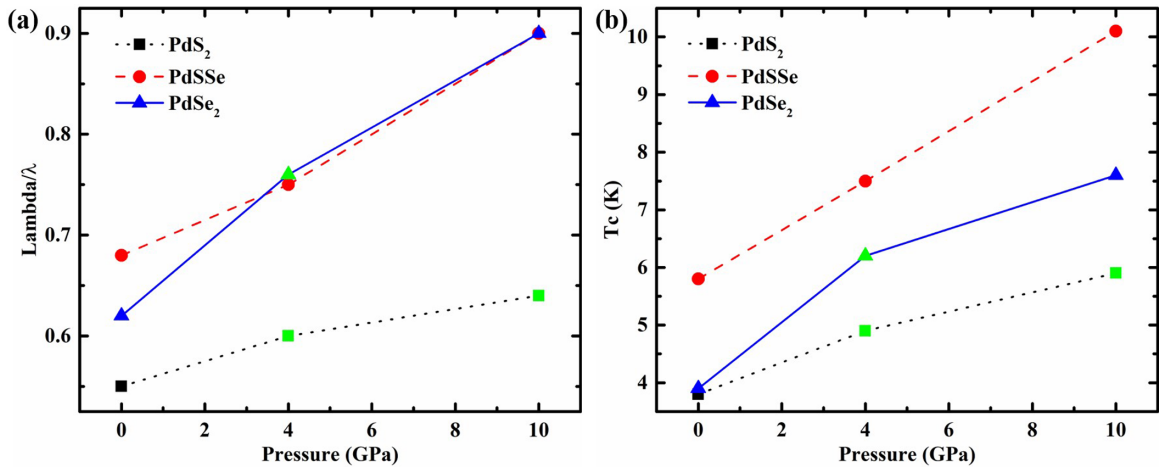

FIG. 6. The evolutions of (a) electron-phonon coupling constants and (b) superconducting critical temperatures of PdS_2, PdSSe, and $PdSe_2$ along with pressure. The data drawn in green come from our previous theoretically calculated results [35].

is not directly correlated with the emergence of superconductivity in the pyrite-type compounds. The topological nontrivial states around the Fermi level and strong electron-phonon coupling might play a crucial role in triggering the superconductivity in the cubic-phase PdSSe under high pressure. Further experimental studies are needed to clarify.

IV. CONCLUSIONS

In conclusion, we have investigated the transformations of crystal structure and the concomitant evolutions of transport properties in PdSSe under hydrostatic pressure. PdSSe shows a similar structural transition and transport behavior to that observed in its sister compounds of PdS_2 and $PdSe_2$. Pressure-induced structural transitions from layered orthorhombic phase to cubic phase through an intermediate phase have been theoretically predicted in PdSSe, accompanied by a series of electronic structure transitions from semiconductor to semimetal to superconductor. Electronic structure and electron-phonon coupling calculations indicated that the superconductivity can be realized in the high-pressure cubic phase, which originated from the strong electron-phonon coupling associated with topological nontrivial states. The present study not only reveals the pressure-induced structural transformations and semiconductor-semimetal-superconductor transitions in PdSSe but also provides insights into the metallization and topological superconducting properties of the TMDC compounds under high pressure, which will attract further experimental and theoretical explorations of interesting physics in TMDCs.

ACKNOWLEDGMENTS

We would like to thank Dr. Xiaoming Zhang and Xiaobo Ma for fruitful discussions. X.M. and J.L. are sponsored by the National Natural Science Foundation of China (Grants No. 11864008, No. 12134018, and No. 11921004) and the Guangxi Natural Science Foundation (Grants No. 2018AD19200 and No. 2019GXNSFGA245006). C.A. is supported by the Foundation for Polish Science through the International Research Agendas program, cofinanced by the European Union within the Smart Growth Operational Program. The computational work in this research was carried out at the Shanxi Supercomputing Center, and the calculations were performed on TianHe-2.

[1] K. S. Novoselov, A. K. Geim, S. V. Morozov, D. Jiang, Y. Zhang, S. V. Dubonos, I. V. Grigorieva, and A. A. Firsov, Electric field effect in atomically thin carbon films, Science **306**, 666 (2004).

[2] K. S. Novoselov, D. Jiang, F. Schedin, T. J. Booth, V. V. Khotkevich, S. V. Morozov, and A. K. Geim, Two-dimensional atomic crystals, Proc. Natl. Acad. Sci. USA **102**, 10451 (2005).

[3] S. Manzeli, D. Ovchinnikov, D. Pasquier, O. V. Yazyev, and A. Kis, 2D transition metal dichalcogenides, Nat. Rev. Mater. **2**, 17033 (2017).

[4] W. Wang, W. Lei, X. Zheng, H. Li, X. Tang, and X. Ming, Electronic structure and phase transition engineering in NbS_2: Crucial role of van der Waals interactions, Chin. Phys. B **29**, 056201 (2020).

[5] L. Pi, L. Li, K. Liu, Q. Zhang, H. Li, and T. Zhai, Recent progress on 2D noble-transition-metal dichalcogenides, Adv. Funct. Mater. **29**, 1904932 (2019).

[6] R. Kempt, A. Kuc, and T. Heine, Two-dimensional noble-metal chalcogenides and phosphochalcogenides, Angew. Chem. Int. Ed. **59**, 9242 (2020).

[7] Y. Wang, J. Pang, Q. Cheng, L. Han, Y. Li, X. Meng, B. Ibarlucea, H. Zhao, F. Yang, H. Liu, H. Liu, W. Zhou, X. Wang, M. H. Rummeli, Y. Zhang, and G. Cuniberti, Applications of 2D-layered palladium diselenide and its van der Waals

heterostructures in electronics and optoelectronics, Nano-Micro Lett. **13**, 143 (2021).

[8] M. A. Pell, Y. V. Mironov, and J. A. Ibers, $PdTe_2$, Acta Crystallogr., Sect. C: Cryst. Struct. Commun. **52**, 1331 (1996).

[9] C. Liu, C. Lian, M. Liao, Y. Wang, Y. Zhong, C. Ding, W. Li, C. Song, K. He, X. Ma, W. Duan, D. Zhang, Y. Xu, L. Wang, and Q. Xue, Two-dimensional superconductivity and topological states in $PdTe_2$ thin films, Phys. Rev. Mater. **2**, 094001 (2018).

[10] F. Gronvold, H. Haraldsen, and A. Kjekshus, On the sulfides, selenides and tellurides of platinum, Acta Chem. Scand. **14**, 1879 (1960).

[11] F. Hulliger, Electrical properties of some nickel-group chalcogenides, J. Phys. Chem. Solids **26**, 639 (1965).

[12] A. A. Puretzky, A. D. Oyedele, K. Xiao, A. V. Haglund, B. G. Sumpter, D. Mandrus, D. B. Geohegan, and L. Liang, Anomalous interlayer vibrations in strongly coupled layered $PdSe_2$, 2D Mater. **5**, 035016 (2018).

[13] J. Sun, H. Shi, T. Siegrist, and D. J. Singh, Electronic, transport, and optical properties of bulk and mono-layer $PdSe_2$, Appl. Phys. Lett. **107**, 153902 (2015).

[14] M. Wei, J. Lian, Y. Zhang, C. Wang, Y. Wang, and Z. Xu, Layer-dependent optical and dielectric properties of large-size $PdSe_2$ films grown by chemical vapor deposition, npj 2D Mater. Appl. **6**, 1 (2022).

[15] H. Kim and H. J. Choi, Quasiparticle band structures of bulk and few-layer $PdSe_2$ from first-principles *GW* calculations, Phys. Rev. B **103**, 165419 (2021).

[16] A. V. Kuklin and H. Ågren, Quasiparticle electronic structure and optical spectra of single-layer and bilayer $PdSe_2$: Proximity and defect-induced band gap renormalization, Phys. Rev. B **99**, 245114 (2019).

[17] A. D. Oyedele, S. Yang, L. Liang, A. A. Puretzky, K. Wang, J. Zhang, P. Yu, P. R. Pudasaini, A. W. Ghosh, Z. Liu, C. M. Rouleau, B. G. Sumpter, M. F. Chisholm, W. Zhou, P. D. Rack, D. B. Geohegan, and K. Xiao, $PdSe_2$: Pentagonal two-dimensional layers with high air stability for electronics, J. Am. Chem. Soc. **139**, 14090 (2017).

[18] L. Lu, G. Chen, H. Cheng, C. Chuu, K. Lu, C. Chen, M. Lu, T. Chuang, D. Wei, W. Chueh, W. Jian, M. Li, Y. Chang, L. Li, and W. Chang, Layer-dependent and in-plane anisotropic properties of low-temperature synthesized few-layer $PdSe_2$ single crystals, ACS Nano **14**, 4963 (2020).

[19] L. Pi, C. Hu, W. Shen, L. Li, P. Luo, X. Hu, P. Chen, D. Li, Z. Li, X. Zhou, and T. Zhai, Highly in-plane anisotropic 2D $PdSe_2$ for polarized photodetection with orientation selectivity, Adv. Funct. Mater. **31**, 2006774 (2021).

[20] Y. Gu, H. Cai, J. Dong, Y. Yu, A. N. Hoffman, C. Liu, A. D. Oyedele, Y. Lin, Z. Ge, A. A. Puretzky, G. Duscher, M. F. Chisholm, P. D. Rack, C. M. Rouleau, Z. Gai, X. Meng, F. Ding, D. B. Geohegan, and K. Xiao, Two-dimensional palladium diselenide with strong in-plane optical anisotropy and high mobility grown by chemical vapor deposition, Adv. Mater. **32**, 1906238 (2020).

[21] D. Qin, P. Yan, G. Ding, X. Ge, H. Song, and G. Gao, Monolayer $PdSe_2$: A promising two-dimensional thermoelectric material, Sci. Rep. **8**, 2764 (2018).

[22] Y. Zhao, P. Yu, G. Zhang, M. Sun, D. Chi, K. Hippalgaonkar, J. T. L. Thong, and J. Wu, Low-symmetry $PdSe_2$ for high performance thermoelectric applications, Adv. Funct. Mater. **30**, 2004896 (2020).

[23] Y. Lan, X. Chen, C. Hu, Y. Cheng, and Q. Chen, Penta-PdX_2 (X = S, Se, Te) monolayers: Promising anisotropic thermoelectric materials, J. Mater. Chem. A **7**, 11134 (2019).

[24] W. L. Chow, P. Yu, F. Liu, J. Hong, X. Wang, Q. Zeng, C. Hsu, C. Zhu, J. Zhou, X. Wang, J. Xia, J. Yan, Y. Chen, D. Wu, T. Yu, Z. Shen, H. Lin, C. Jin, B. K. Tay, and Z. Liu, High mobility 2D palladium diselenide field-effect transistors with tunable ambipolar characteristics, Adv. Mater. **29**, 1602969 (2017).

[25] W. Lei, B. Cai, H. Zhou, G. Heymann, X. Tang, S. Zhang, and X. Ming, Ferroelastic lattice rotation and band-gap engineering in quasi 2D layered-structure $PdSe_2$ under uniaxial stress, Nanoscale **11**, 12317 (2019).

[26] B. Wei, J. Liu, Q. Cai, A. Alatas, A. H. said, C. Li, and J. Hong, Giant anisotropic in-plane thermal conduction induced by anomalous phonons in nearly-equilaterally structured $PdSe_2$, Mater. Today Phys. **22**, 100599 (2022).

[27] P. Lv, G. Tang, Y. Liu, Y. Lun, X. Wang, and J. Hong, Van der Waals direction transformation induced by shear strain in layered $PdSe_2$, Extreme Mech. Lett. **44**, 101231 (2021).

[28] L. Zeng, D. Wu, S. Lin, C. Xie, H. Yuan, W. Lu, S. P. Lau, Y. Chai, L. Luo, Z. Li, and Y. H. Tsang, Controlled synthesis of 2D palladium diselenide for sensitive photodetector applications, Adv. Funct. Mater. **29**, 1806878. (2019).

[29] Q. Liang, Q. Wang, Q. Zhang, J. Wei, S. X. Lim, R. Zhu, J. Hu, W. Wei, C. Lee, C. Sow, W. Zhang, and A. T. S. Wee, High-performance, room temperature, ultra-broadband photodetectors based on air-stable $PdSe_2$, Adv. Mater. **31**, 1807609 (2019).

[30] J. Yu, X. Kuang, J. Li, J. Zhong, C. Zeng, L. Cao, Z. Liu, Z. Zeng, Z. Luo, T. He, A. Pan, and Y. Liu, Giant nonlinear optical activity in two-dimensional palladium diselenide, Nat. Commun. **12**, 1083 (2021).

[31] A. D. Bartolomeo, A. Pelella, X. Liu, F. Miao, M. Passacantando, F. Giubileo, A. Grillo, L. Iemmo, F. Urban, and S. Liang, Pressure-tunable ambipolar conduction and hysteresis in thin palladium diselenide field effect transistors, Adv. Funct. Mater. **29**, 1902483 (2019).

[32] Y. Gao, X. Liu, W. Hu, and J. Yang, Tunable n-type and p-type doping of two-dimensional layered $PdSe_2$ via organic molecular adsorption, Phys. Chem. Chem. Phys. **22**, 12973 (2020).

[33] M. A. ElGhazali, P. G. Naumov, Q. Mu, V. Süß, A. O. Baskakov, C. Felser, and S. A. Medvedev, Pressure-induced metallization, transition to the pyrite-type structure, and superconductivity in palladium disulfide PdS_2, Phys. Rev. B **100**, 014507 (2019).

[34] C. Soulard, X. Rocquefelte, P. E. Petit, M. Evain, S. Jobic, J. P. Itié, P. Munsch, H. J. Koo, and M. H. Whangbo, Experimental and theoretical investigation on the relative stability of the PdS_2-and pyrite-type structures of $PdSe_2$, Inorg. Chem. **43**, 1943 (2004).

[35] W. Lei, W. Wang, X. Ming, S. Zhang, G. Tang, X. Zheng, H. Li, and C. Autieri, Structural transition, metallization, and superconductivity in quasi-two-dimensional layered PdS_2 under compression, Phys. Rev. B **101**, 205149 (2020).

[36] M. A. ElGhazali, P. G. Naumov, H. Mirhosseini, V. Süß, L. Müchler, W. Schnelle, C. Felser, and S. A. Medvedev, Pressure-induced superconductivity up to 13.1 K in the pyrite phase of palladium diselenide $PdSe_2$, Phys. Rev. B **96**, 060509(R) (2017).

[37] W. Lei, S. Zhang, G. Heymann, X. Tang, J. Wen, X. Zheng, G. Hua, and X. Ming, A new 2D high-pressure phase of $PdSe_2$ with high-mobility transport anisotropy for photovoltaic applications, J. Mater. Chem. C **7**, 2096 (2019).

[38] W. Zhang, Y. Cui, C. Zhu, B. Huanga, and S. Yana, Flexible ferroelasticity in monolayer PdS_2: A DFT study, Phys. Chem. Chem. Phys. **23**, 10551 (2021).

[39] D. Raval, B. Babariya, S. K. Gupta, P. N. Gajjar, and R. Ahuja, Ultrahigh carrier mobility and light-harvesting performance of 2D penta-PdX_2 monolayer, J. Mater. Sci. **56**, 3846 (2021).

[40] Y. Wang and J. Ren, Strain-driven switchable thermal conductivity in ferroelastic $PdSe_2$, ACS Appl. Mater. Interfaces **13**, 34724 (2021).

[41] W. Luo, A. D. Oyedele, Y. Gu, T. Li, X. Wang, A. V. Haglund, D. Mandrus, A. A. Puretzky, K. Xiao, L. Liang, and X. Ling, Anisotropic phonon response of few-layer $PdSe_2$ under uniaxial strain, Adv. Funct. Mater. **30**, 2003215 (2020).

[42] A. D. Oyedele, S. Yang, T. Feng, A. V. Haglund, Y. Gu, A. A. Puretzky, D. Briggs, C. M. Rouleau, M. F. Chisholm, R. R. Unocic, D. Mandrus, H. M. Meyer III, S. T. Pantelides, D. B. Geohegan, and K. Xiao, Defect-mediated phase transformation in anisotropic two-dimensional $PdSe_2$ crystals for seamless electrical contacts, J. Am. Chem. Soc. **141**, 8928 (2019).

[43] G. D. Nguyen, L. Liang, Q. Zou, M. Fu, A. D. Oyedele, B. G. Sumpter, Z. Liu, Z. Gai, K. Xiao, and A. Li, 3D Imaging and Manipulation of Subsurface Selenium Vacancies in $PdSe_2$, Phys. Rev. Lett. **121**, 086101 (2018).

[44] J. Lin, S. Zuluaga, P. Yu, Z. Liu, S. T. Pantelides, and K. Suenaga, Novel Pd_2Se_3 Two-Dimensional Phase Driven by Interlayer Fusion in Layered $PdSe_2$, Phys. Rev. Lett. **119**, 016101 (2017).

[45] X. Liu, Y. Wang, Q. Guo, S.-J. Liang, T. Xu, B. Liu, J. Qiao, S. Lai, J. Zeng, S. Hao, C. Gu, T. Cao, C. Wang, Y. Wang, C. Pan, G. Su, Y. Nie, X. Wan, L. Sun, Z. Wang, L. He, B. Cheng, and F. Miao, Temperature-sensitive spatial distribution of defects in $PdSe_2$ flakes, Phys. Rev. Mater. **5**, L041001 (2021).

[46] W. Liu, M. R. Osanloo, X. Wang, S. Li, N. Dhale, H. Wu, M. L. V. d. Put, S. Tiwari, W. G. Vandenberghe, and B. Lv, New verbeekite-type polymorphic phase and rich phase diagram in the $PdSe_{2-x}Te_x$ system, Phys. Rev. B **104**, 024507 (2021).

[47] J. H. Ryua, K. H. Leeb, S. Hong, J. Y. Hwang, Y. Yi, S. Im, S. Kim, S. Y. Kim, and K. Lee, Compositional effect in pentagonal layered $PdSe_{2-x}S_x$ solid-solutions and their transport properties, Scr. Mater. **182**, 6 (2020).

[48] S. H. Zhang and B. G. Liu, Hole-doping-induced half-metallic ferromagnetism in a highly-air-stable $PdSe_2$ monolayer under uniaxial stress, J. Mater. Chem. C **6**, 6792 (2018).

[49] Q. Liang, Q. Zhang, J. Gou, T. Song, H. Chen Arramel, M. Yang, S. X. Lim, Q. Wang, R. Zhu, N. Yakovlev, S. C. Tan, W. Zhang, K. S. Novoselov, and A. T. S. Wee, Performance improvement by ozone treatment of 2D $PdSe_2$, ACS Nano **14**, 5668 (2020).

[50] R. Sun, S. Jin, J. Deng, M. Hao, X. Zhong, Y. Ma, M. Li, and X. Chen, Chemical pressure boost record-high superconductivity in van der Waals materials $FeSe_{1-x}S_x$, Adv. Funct. Mater. **31**, 2102917 (2021).

[51] W. Liu, S. Li, H. Wu, N. Dhale, P. Koirala, and B. Lv, Enhanced superconductivity in the Se-substituted 1T-$PdTe_2$, Phys. Rev. Mater. **5**, 014802 (2021).

[52] F. Xiao, W. Lei, W. Wang, L. Xu, S. Zhang, and X. Ming, Pentagonal two-dimensional noble-metal dichalcogenide PdSSe for photocatalytic water splitting with pronounced optical absorption and ultrahigh anisotropic carrier mobility, J. Mater. Chem. C **9**, 7753 (2021).

[53] Y. Zhou, X. Yang, and J. He, PdSSe: Two-dimensional pentagonal Janus structures with strong visible light absorption for photovoltaic and photocatalytic applications, Vacuum **181**, 109649 (2020).

[54] G. Kresse and J. Furthmüller, Efficient iterative schemes for ab initio total-energy calculations using a plane-wave basis set, Phys. Rev. B **54**, 11169 (1996).

[55] G. Kresse and J. Furthmüller, Efficiency of ab-initio total energy calculations for metals and semiconductors using a plane-wave basis set, Comput. Mater. Sci. **6**, 15 (1996).

[56] J. P. Perdew, K. Burke, and M. Ernzerhof, Generalized Gradient Approximation Made Simple, Phys. Rev. Lett. **77**, 3865 (1996).

[57] J. Heyd, G. E. Scuseria, and M. Ernzerhof, Hybrid functionals based on a screened Coulomb potential, J. Chem. Phys. **118**, 8207 (2003).

[58] A. V. Krukau, O. A. Vydrov, A. F. Izmaylov, and G. E. Scuseria, Influence of the exchange screening parameter on the performance of screened hybrid functionals, J. Chem. Phys. **125**, 224106 (2006).

[59] P. Giannozzi, S. Baroni, N. Bonini, M. Calandra, R. Car, C. Cavazzoni, D. Ceresoli, G. L. Chiarotti, M. Cococcioni, I. Dabo, A. D. Corso, S. d. Gironcoli, S. Fabris, G. Fratesi, R. Gebauer, U. Gerstmann, C. Gougoussis, A. Kokalj, M. Lazzeri, L. Martin-Samos, N. Marzari, F. Mauri, R. Mazzarello, S. Paolini, A. Pasquarello, L. Paulatto, C. Sbraccia, S. Scandolo, G. Sclauzero, A. P. Seitsonen, A. Smogunov, P. Umari, and R. M. Wentzcovitch, QUANTUM ESPRESSO: A modular and open-source software project for quantum simulations of materials, J. Phys.: Condens. Matter **21**, 395502 (2009).

[60] See Supplemental Material at http://link.aps.org/supplemental/10.1103/PhysRevB.105.115110 for the convergence test of the parameters of cut-off energy and k points used in vasp/QE; evolutions of the lattice constants for *AA* polymorph PdSSe under pressure calculated by standard PBE and LDA functionals without considering the vdW corrections; the choice of the semiempirical correction methods; the evolution of distortive degree (Δ_d) with hydrostatic pressure; the calculated phonon spectrum and band structures of the cubic PdSSe at 4 GPa calculated by the PBE+dDsC, PBE, and LDA functionals; band gaps of PdSSe under compression calculated with HSE06 functionals; enlarged band structures of the intermediate phase PdSSe (*AA* polymorph) at pressure of 3.5 GPa; DOS evolutions for the three polymorphs PdSSe from the ambient orthorhombic phase to high-pressure phase at 4 GPa; the projected band structure and the corresponding Fermi surface and the enlarged image of the Weyl points of the high-pressure cubic phase PdSSe (*AA* polymorph) at 4 GPa; results and discussions on the crystal structure and electronic structural evolution of the *AB* and *BB* polymorphs under hydrostatic pressure; as well as the electronic structure and superconductivity of the high-pressure-phase PdSSe.

[61] P. B. Allen and R. C. Dynes, Transition temperature of strong-coupled superconductors reanalyzed, Phys. Rev. B. **12**, 905 (1975).

[62] W. Wang, B. Wang, Z. Gao, G. Tang, W. Lei, X. Zheng, H. Li, X. Ming, and C. Autieri, Charge density wave instability and pressure-induced superconductivity in bulk 1T-NbS_2, Phys. Rev. B **102**, 155115 (2020).

[63] W. Wang, C. Si, W. Lei, F. Xiao, Y. Liu, C. Autieri, and X. Ming, Stacking order and Coulomb correlation effect in the layered charge density wave phase of 1T-NbS_2, Phys. Rev. B **105**, 035119 (2022).

[64] S. N. Steinmann and C. Corminboeuf, A generalized-gradient approximation exchange hole model for dispersion coefficients, J. Chem. Phys. **134**, 044117 (2011).

[65] S. N. Steinmann and C. Corminboeuf, Comprehensive benchmarking of a density-dependent dispersion correction, J. Chem. Theory Comput. **7**, 3567 (2011).

[66] S. S. Batsanov, Van der Waals radii of elements, Inorg. Mater. **37**, 871 (2001).

[67] B. Cordero, V. Gómez, A. E. Platero-Prats, M. Revés, J. Echeverría, E. Cremades, F. Barragána, and S. Alvarez, Covalent radii revisited, Dalton Trans. 2832 (2008).

[68] I. D. Brown and R. D. Shannon, Empirical bond-strength–bond-length curves for oxides, Acta Crystallogr., Sect. A: Cryst. Phys., Diffr., Theor. Gen. Crystallogr. **29**, 266 (1973).

[69] Q. Dong, Q. Li, S. Li, X. Shi, S. Niu, S. Liu, R. Liu, B. Liu, X. Luo, J. Si, W. Lu, N. Hao, Y. Sun, and B. Liu, Structural phase transition and superconductivity hierarchy in 1T-TaS_2 under pressure up to 100 GPa, npj Quantum Mater. **6**, 1 (2021).

[70] X. Ming, C. Autieri, K. Yamauchi, and S. Picozzi, Role of square planar coordination in the magnetic properties of Na_4IrO_4, Phys. Rev. B **96**, 205158 (2017).

[71] M. Kakihana, A. Teruya, K. Nishimura, A. Nakamura, T. Takeuchi, Y. Haga, H. Harima, M. Hedo, T. Nakama, and Y. Ōnuki, Split Fermi surface properties in ullmannite NiSbS and PdBiSe with the cubic chiral crystal structure, J. Phys. Soc. Jpn. **84**, 094711 (2015).

[72] A. Furusaki, Weyl points and Dirac lines protected by multiple screw rotations, Sci. Bull. **62**, 788 (2017).

[73] B. Bradlyn, J. Cano, Z. Wang, M. G. Vergniory, C. Felser, R. J. Cava, and B. A. Bernevig, Beyond Dirac and Weyl fermions: Unconventional quasiparticles in conventional crystals, Science **353**, aaf5037 (2016).

[74] M. G. Vergniory, L. Elcoro, C. Felser, N. Regnault, B. A. Bernevig, and Z. Wang, A complete catalogue of high-quality topological materials, Nature (London) **566**, 480 (2019).

[75] R. Slager, A. Mesaros, V. Juričić, and J. Zaanen, The space group classification of topological band-insulators, Nat. Phys. **9**, 98 (2013).

[76] J. Kruthoff, J. d. Boer, J. v. Wezel, C. L. Kane, and R. Slager, Topological Classification of Crystalline Insulators through Band Structure Combinatorics, Phys. Rev. X **7**, 041069 (2017).

[77] M. G. Vergniory, B. J. Wieder, L. Elcoro, S. S. P. Parkin, C. Felser, B. A. Bernevig, and N. Regnault, All topological bands of all stoichiometric materials, arXiv:2105.09954.

[78] Y. Yin, M. S. Fuhrer, and N. V. Medhekar, Selective control of surface spin current in topological pyrite-type OsX_2 (X = Se, Te) crystals, npj Quantum Mater. **4**, 47 (2019).

[79] S. Friedemann, H. Chang, M. Gamża, P. Reiss, X. Chen, P. Alireza, W. Coniglio, D. Graf, S. Tozer, and F. M. Grosche, Large Fermi surface of heavy electrons at the border of Mott insulating state in NiS_2, Sci. Rep. **6**, 25335 (2016).

[80] A. Teruya, F. Suzuki, D. Aoki, F. Honda, A. Nakamura, M. Nakashima, Y. Amako, H. Harima, M. Hedo, T. Nakama, and Y. Ōnuki, Large cyclotron mass and large ordered moment in ferromagnet CoS_2 compared with paramagnet $CoSe_2$, J. Phys. Soc. Jpn. **85**, 064716 (2016).

[81] Z. Li, G. Antonius, M. Wu, F. H. d. Jornada, and S. G. Louie, Electron-Phonon Coupling from Ab Initio Linear-Response Theory within the *GW* Method: Correlation-Enhanced Interactions and Superconductivity in $Ba_{1-x}K_xBiO_3$, Phys. Rev. Lett. **122**, 186402 (2019).

[82] X. Liang, A. Bergara, Y. Xie, L. Wang, R. Sun, Y. Gao, X. Zhou, B. Xu, J. He, D. Yu, G. Gao, and Y. Tian, Prediction of superconductivity in pressure-induced new silicon boride phases, Phys. Rev. B **101**, 014112 (2020).

[83] A. Majumdar, J. S. Tse, M. Wu, and Y. Yao, Superconductivity in FeH_5, Phys. Rev. B **96**, 201107(R) (2017).